



Three-dimensional high resolution X-ray imaging and quantification of lithium ion battery mesocarbon microbead anodes



F. Tariq^{a,*}, V. Yufit^a, M. Kishimoto^a, P.R. Shearing^b, S. Menkin^c, D. Golodnitsky^c, J. Gelb^d, E. Peled^c, N.P. Brandon^a

^a Department of Earth Science and Engineering, Imperial College London, SW7 2AZ, UK

^b Department of Chemical Engineering, University College London, WC1E 7JE, UK

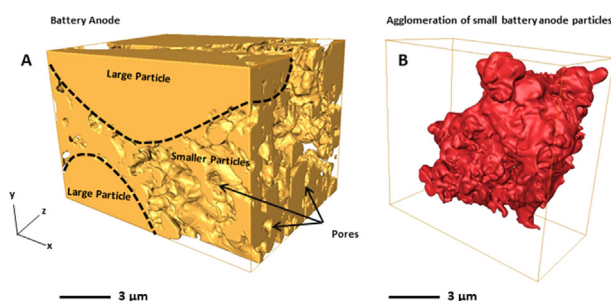
^c School of Chemistry, Tel Aviv University, Tel Aviv 69978, Israel

^d Xradia Inc., Pleasanton, CA 94588, USA

HIGHLIGHTS

- High resolution 3D nano-CT was used to image MCMB anodes down to 16 nm voxel size.
- A specimen labelling methodology was used to enhance image contrast.
- The 3D MCMB anode had a heterogeneous and bi-modally distributed microstructure.
- Anode was quantified via surface area, volume, connectivity and tortuosity factors.
- Complexity of both MCMB and electrolyte phases suggests inhomogeneous anode use.

GRAPHICAL ABSTRACT



ARTICLE INFO

Article history:

Received 14 June 2013

Received in revised form

4 August 2013

Accepted 30 August 2013

Available online 11 October 2013

Keywords:

Lithium ion batteries

Microstructure

MCMB

X-ray tomography

Anode

ABSTRACT

In order to improve lithium ion batteries it is important to characterise real electrode geometries and understand how their 3D structure may affect performance. In this study, high resolution synchrotron nano-CT was used to acquire 3D tomography datasets of mesocarbon microbead (MCMB) based anodes down to a 16 nm voxel size. A specimen labelling methodology was used to produce anodes that enhance the achievable image contrast, and image processing routines were utilised to successfully segment features of interest from a challenging dataset. The 3D MCMB based anode structure was analysed revealing a heterogeneous and bi-modally distributed microstructure. The microstructure was quantified through calculations of surface area, volume, connectivity and tortuosity factors. In doing so, two different methods, random walk and diffusion based, were used to determine tortuosity factors of both MCMB and pore/electrolyte microstructures. The tortuosity factors (2–7) confirmed the heterogeneity of the anode microstructure for this field of view and demonstrated small MCMB particles interspersed between large MCMB particles cause an increase in tortuosity factors. The anode microstructure was highly connected, which was also caused by the presence of small MCMB particles. The complexity in microstructure suggests inhomogeneous local lithium ion distribution would occur within the anode during operation.

© 2013 Elsevier B.V. All rights reserved.

* Corresponding author.

E-mail address: farid.tariq02@imperial.ac.uk (F. Tariq).

1. Introduction

Meeting increasing energy demands, storage requirements and energy portability will be expedited through an ability to directly image battery micro/nano structures at high resolutions in three dimensions (3D). In doing so, it is possible to relate battery structure with behaviour. An ability to circumvent current contrast limitations when imaging state-of-the-art lithium ion battery electrodes and quantify them provides an important step towards achieving this goal. This capability offers the future optimisation of lithium ion batteries through better microstructure designs.

A typical lithium ion battery consists of three components; a graphite based anode, metal oxide cathode and a separator composed of a polymer and organic electrolyte. It is beyond the scope of the paper to review different bulk and surface processes responsible for battery functioning, ageing or failure. Nonetheless it is well known that some of these bulk processes are associated with structural transformation of the solid phase of battery electrodes and that in certain cases (e.g. or Sn electrodes) they can induce large volumetric expansions of up to 300% [1]. Other processes are linked to the surface reactions between lithium and electrolyte to form a thin, passive solid electrolyte interphase (SEI) film [2,3]. Therefore the microstructure of the electrodes will affect, and also be affected by, these processes.

The effects of electrode microstructure on cell level performance and degradation have been widely acknowledged, however it is only relatively recently that the availability of high resolution tomography tools have enabled the capture of complex 3D geometry of battery electrodes with sufficient detail. Recent studies present the application of focused ion beam tools [4–6] as well as laboratory and synchrotron X-ray CT [7–10] to resolve electrode structures into 3D, and these data have also been successfully combined with modelling tools to explore the relationship between microstructure and performance [11,12]. In this paper we report the application of nano-scale resolution X-Ray tomography to study the microstructure of graphite-based electrode materials and then quantify both the pore and MCMB phases.

Until now, imaging of graphite particles at sub-100 nm resolution in 3D has been difficult due to (i) the low X-ray attenuation coefficient of graphite and (ii) the interaction of graphite with focused ion beams, which can lead to highly non-uniform nano-scale milling. Therefore the precise nanostructure of graphite-based anodes at high resolution has been poorly understood. This paper applies a labelling technique to improve contrast between the polymer binder and the electroactive mesocarbon microbead (MCMB) particles used for lithium ion battery anodes. As the labelled binder coats MCMB particles during anode fabrication, this also helps in the identification of MCMB particle edges. The use of MCMB particles is also useful for simulation purposes due to their sphericity [13,14]. We demonstrate here a methodology to obtain 3D micro/nano structural information of battery anodes and use it to characterise complex anode geometries, and thereby begin to understand how they function. In doing so, new insights are gained that could be used to develop improved anode designs.

2. Experimental

X-ray nano-tomography (nano-CT) involves using an X-ray beam to produce a series of transmission projection images of an object as it is rotated through multiple angles (Fig. 1). The resulting contrast in each acquired image is a function of the attenuation coefficients or interference effects of the phases through which the X-ray is transmitted. While X-ray sources themselves may be laboratory based, synchrotron X-ray sources provide parallel, monochromatic illumination with both good signal-to-noise and high-resolution capabilities [15]. The validity of X-ray tomography as a technique in imaging battery electrodes has been demonstrated in several studies [7,16,17]. As nano-CT instruments have a limited field of view, samples must be carefully prepared to ensure they fit within it [18].

Graphite anode mesocarbon microbeads (MCMB 6-28, Osaka Gas Co.) particles were fabricated in the following manner: an anhydrous LiI salt (Sigma–Aldrich) used as a labelling agent and polyethylene oxide (PEO, Sigma–Aldrich, 5×10^6 M.W.) was dissolved in acetonitrile followed by addition of the corresponding amount of MCMB graphite. The resulting solution was then cast on thin copper foil. The final composition of the anode consisted of 88w/w MCMB, 10w/w PEO and 2w/w LiI. LiI was selected due to presence of heavy iodide ion that creates a contrast between graphite and the binder for X-rays. The PEO is known for its ability to dissolve LiI and form solid state complexes with various stoichiometry [19]. Similarly, the iodine-based compounds, called radiocontrasts, are widely used in medical CT [20]. It is worth noting the PEO binder was selected to serve as a complexing agent for LiI which cannot be achieved using more conventional binders based on polyvinylidene fluoride (PVDF). Although PEO is not a common binder it can be used as a binder for both cathode and anode fabrication [21]. For further details concerning PEO and LiI the reader is referred to other studies [22–29].

Following preparation, the MCMB sample was imaged in scanning electron mode using a Zeiss Auriga dual beam (FIBSEM) microscope with an accelerating voltage of 2 kV. X-ray imaging was subsequently conducted using an Xradia nanoXCT-S100 TXM at synchrotron beamline 6-2-C at the Stanford Synchrotron Radiation Lightsource (SSRL), Stanford, USA (Fig. 1). A field of view of $\sim 15 \times 15 \times 12 \mu\text{m}$ was acquired with 721 transmission images taken at 0.5° rotation intervals using 6.5 keV incident X-ray beam energy. The transmission images were reconstructed using a standard parallel beam filtered back-projection algorithm (Xradia Reconstructor) producing a final dataset with isotropic voxel size ca. 16 nm following alignments and reconstruction.

The acquired grey-scale 3D datasets were analysed using image processing techniques to segment MCMB particles and porous (electrolyte) regions out of the bulk volume. The anode structure was then evaluated using both commercial and in-house routines by calculating surface areas, volume fractions and tortuosity factors. Further details are provided in subsections of the paper.

Image analysis techniques had to be applied in order to segment and quantify the 3D imaged data. The general procedure involves

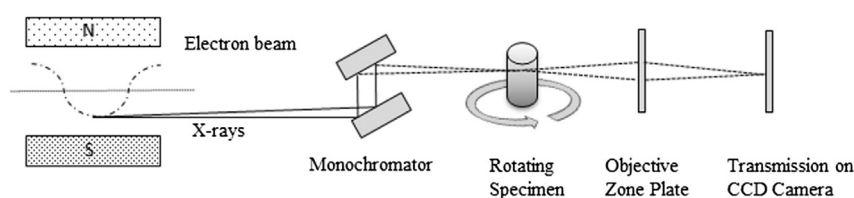


Fig. 1. The X-ray nano-tomography beam-line setup at 6-2-C at SSRL. Samples are rotated relative to the source-detectors with field of view determined by post-sample Fresnel zone plates that focus X-rays prior to the CCD camera.

conversion of 3D grey-scale datasets into segmented volumes based on boundary values that best represent features of interest as observed in their original dataset as detailed in prior studies [30–34]. Although many standard image processing techniques are cited in the literature [32,33], image processing must also be tailored towards the requirements of a particular dataset or towards features of interest. Therefore, after the dataset was acquired, in order to overcome contrast and artifact issues, a number of steps were carried out using a wide range of tools (Avizo, VSG, [35]/ImageJ [36]/ITK [30,37]). Consequently, a combinatory approach was used to help select features of interest from the anode nano-CT data, as detailed subsequently.

3. Results and discussion

3.1. Contrast enhancing labelling

Secondary electron images of the MCMB structure (Fig. 2) reveal a particle distribution of many different sizes. Small particles with micron and sub-micron radii decorate larger particles of ca. 3 μm radii and fill the spaces between them. The structure therefore appears bi-modally sized. However, limitations of SEM preclude more comprehensive understanding of anode structure in three dimensions. Only the presently revealed face can be directly imaged in 2D. This makes understanding the true connectivity of particles, and also interfaces between them difficult to study. Uniquely X-ray nano-CT can provide this information in a complementary fashion and is a non-destructive technique. Fig. 2 illustrates an analogous region of the anode that was imaged using high resolution synchrotron X-ray analysis, while meeting field of view (FOV) requirements as FOV decreases with high X-ray resolution.

Following tomographic reconstruction, the image clearly shows it is possible to demarcate edges between solid and pore space using X-ray nano-CT, Lil, and this imaging methodology, as shown in Fig. 3 for a single slice from the 3D anode dataset. 3D X-ray imaging has been traditionally difficult for battery anodes owing to the low atomic number of carbon. However, high resolution data down to a voxel size of 16 nm with sub-100 nm features visible was successfully acquired. This anode data revealed the presence of smaller MCMB particles occupying space between larger MCMB

particles representing information that is not visible at coarser and more typically available X-ray resolutions ($>1\text{--}2\text{ }\mu\text{m}$). This correlates well with SEM based images (Fig. 2) of the same structure. However, unlike SEM, from Fig. 3 it is possible to directly image the interfaces between particles and pores for the entire volume analysed. This in turn can reveal surface areas, volume sizes, connectivity and the tortuosity factors of the anode at sub-100 nm resolution not possible with 2D imaging.

During anode manufacture, labelling was utilised to enhance X-ray image contrast and permit the location of binder to be analysed (contrast enhancing labelling). Although the current image contrast was not sufficient to reliably distinguish all binder locations from active MCMB particles, the small rounded bright particles (typically $\sim 0.25\text{ }\mu\text{m}$ diameter size) within the dataset are likely to be binder (PEO–Lil complex) and/or undissolved Lil. The binder coats the MCMB particulate surface with ca. 70–150 nm thickness producing bright edges. From earlier studies it is known that binder uniformly distributes itself in the anode with only small insoluble particles precipitating out, and this appears consistent with this data [19]. From the current results, binder coatings with $<70\text{ nm}$ thickness around MCMB particles become difficult to discern.

3.2. Image analysis

The data was segmented and labelled according to the phase it represents (MCMB and pore/electrolyte). For the anode dataset, the largest suitable region ($\sim 11 \times 10 \times 10\text{ }\mu\text{m}$) was selected from the tomographic reconstruction for this process. Binarisation of this “raw” data to separate both pore (electrolyte) and MCMB particle structure was challenging as low contrast difference exists between these different phases despite having regions with well-defined edges. The schematic in Fig. 4a illustrates the approach that was implemented for segmenting, with Fig. 4b and c showing the original and segmented data respectively.

The approach shown in Fig. 4a was utilised as it addressed a number of contrast issues as shown in Fig. 3. These issues are chiefly (i) poor contrast between different phases (pore and MCMB particles), (ii) uneven contrast both in-plane and through stack and (iii) X-ray imaging artifacts in the form of streaks. It is apparent from Fig. 3 that the edges between phases are better defined than the phases themselves. Human visual acuity in resolving particle edges occurs from an ability to (i) use a multi-resolution approach across the image in determining the significance of contrast/brightness changes and (ii) comprehend sudden contrast inversions (i.e. edges changing black \rightarrow white and vice versa) with the morphology of the particle itself. However, imaging algorithms are far less accurate in making decisions on what may or may not constitute particles or edges [33].

The approach in Fig. 4a addressed these through firstly a non-linear diffusion filter that was applied to reduce noise and small scale contrast variations within the particles, while preserving particle edges. This was subsequently followed by a background removal filter, which served to reduce uneven background contrast gradients within the images. The result was averaged with the original MCMB dataset to restore some lost edge information, followed by a contrast equalisation filter and image contrast inversion to produce particles and bulk with different contrasts levels suitable for final segmentation. Subsequently, intensity based segmentation was performed to separate MCMB particles from the pore region. In regions where segmentation of the desired phase was non-ideal, an in-house watershed based algorithm [38] was applied and combined with the segmented data, with some under/over-selected regions corrected manually following comparison against the original dataset to produce Fig. 4c.

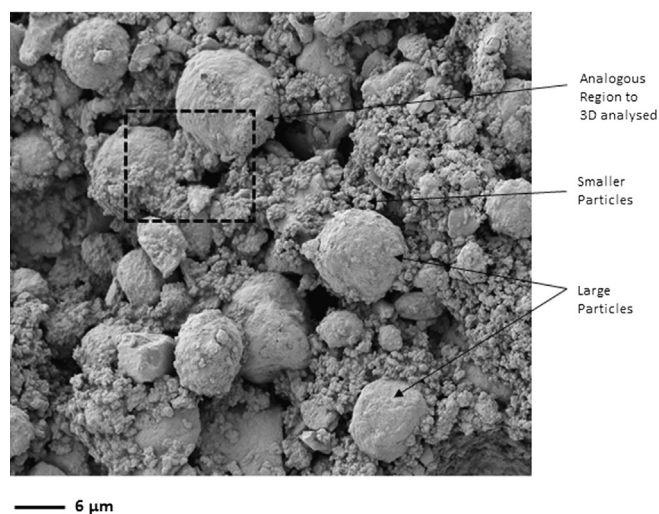


Fig. 2. MCMB graphite anode microstructure following SEM imaging in secondary electron mode. The presence of small and large particles can be observed, alongside a region analogous to that imaged using synchrotron X-ray nano-CT.

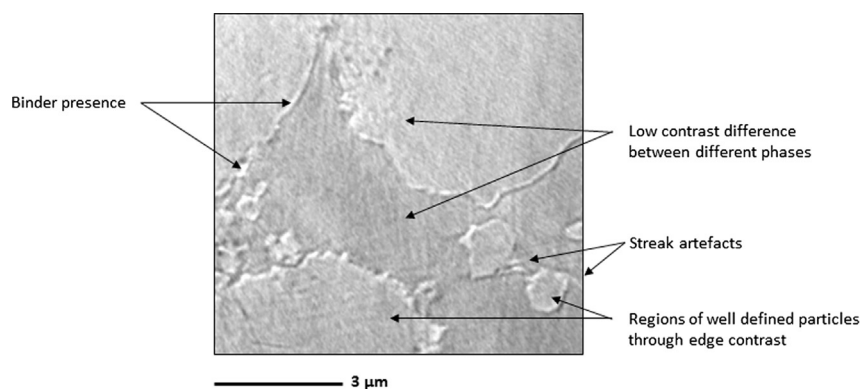


Fig. 3. Example of MCMB graphite anode microstructure following reconstruction with typical image segmentation issues. While some MCMB graphite particle edges are well defined, there is low contrast difference between different phases and subtle changes in image brightness/contrast altogether preventing simple segmentation. A single 2D slice from a sub-section of the 3D volume is shown.

The 3D volume of MCMB anode particle structures are shown in Fig. 4d. The reconstruction encompasses many sets of small particles within the field of view that are well described, making them suitable for further quantitative analysis. Such analysis can consist of deriving useful performance-related metrics or modelling behaviour of real structures. Image processing demonstrated here shows that through a combinatory approach using a number of image processing strategies, it is possible to extract the 3D structure of MCMB anode particles for further examination from challenging datasets.

3.3. Analysis of MCMB graphite anode micro/nano structure

Analysis of the MCMB based anode (Figs. 4 and 5) reveals that it consists of bi-modal MCMB particles visible at this resolution, with the anode MCMB structure spanning across tens of nanometers up to microns in length scale. This is consistent with simpler 2D SEM image based analysis (Fig. 2). Two sets of MCMB particles can be identified corresponding to their typical measured diameters from the 3D dataset (Fig. 5). Large MCMB particles can be seen with ca. 4–6 μm diameters whereas small MCMB particles possess ca. 1–3 μm diameters or less. The 3D imaging results show surface features and undulations of all MCMB particles are on the order of hundreds of nanometers. Both large and small particles are assumed to be MCMB as they possess nearly identical image contrast, unlike LiI doped binder, and their size is larger than typical binder agglomerations [39] and the volume is too large compared with total binder volume (~ 9.3 vol.%). Finally, from earlier studies [19] it is also known most binder forms a coating distributed across MCMB particles surfaces as a result of the anode preparation

routine. Additional analysis of the reconstructed anode volume reveals that small MCMB graphite particles are found occupying spaces between larger adjacent particles. Consequently they also impart good connectivity to the anode microstructure through offering several alternative pathways for ionic diffusion and electronic conductivity. Quantified values can be found in Tables 1–3.

However, due to field of view limitations the 3D MCMB dataset only partly describes larger MCMB graphite particles. Therefore, smaller (ca. 1–3 μm) MCMB graphite particle may be reconstructed more completely than the largest particles (Fig. 5A and B).

The tomography results show the presence of very small particles (less than ca. 0.25–0.5 μm diameters) that appear exceptionally bright. Given their shape and structure these particles are unlikely to be imaging artifacts and more attributable to the presence of small quantities of agglomerated binder/salt. PEO binder is likely to be uniformly distributed along with LiI in the anode, with only small insoluble particles precipitating out, as appears consistent with the current dataset and shown in other studies [19]. In reality, binder is also distributed across MCMB particle surfaces, becoming indistinguishable from MCMB at ca. 50–70 nm thickness and invisible at <16 nm voxel size. However, while additional analysis of the anode is required for better compositional differentiation between the smallest particles, to determine whether they are active or binder, for the purposes of further analysis in this study all the structure is considered as being electrochemically active MCMB particles.

The reconstruction reveals that particles are not perfectly spherical, which can cause differences between predictions in standardised battery models and experimental results [13,14] (Fig. 5). The large diameter MCMB graphite particles appear

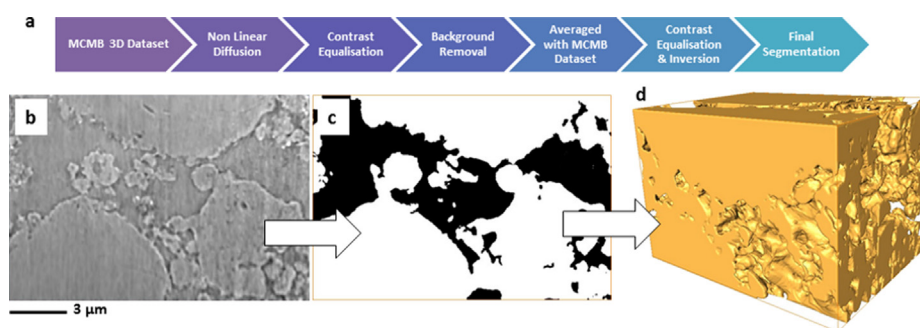


Fig. 4. (a) Schematic of the segmentation approach (b) an original reconstructed slice from synchrotron X-ray nano-CT of MCMB based battery anode (c) segmented MCMB structure following feature extraction (both b and c show 2D slices from a 3D dataset) (d) rendering of the 3D battery anode microstructure following segmentation. The particles are well described and suitable for further analysis.

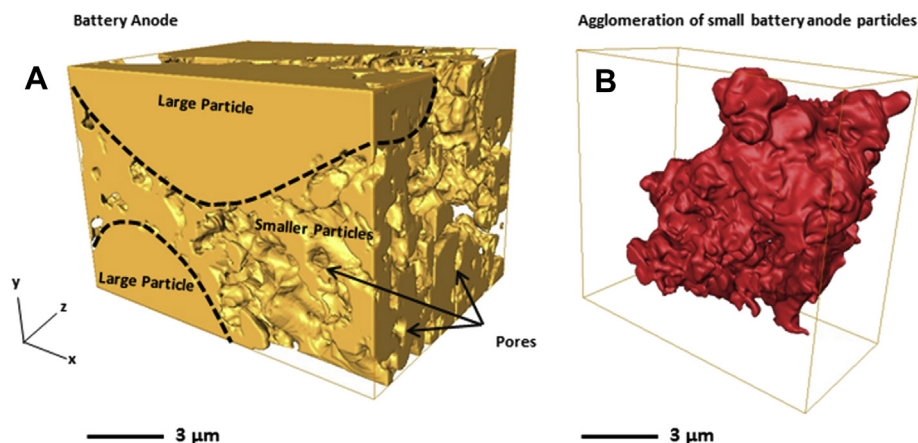


Fig. 5. (A) 3D MCMB based battery anode microstructure. The presence of both large particles and small particles is evident; with no particles being truly spherical. There is good connectivity with smaller particles occupying spaces between the larger particles (B) microstructure of an agglomeration of smaller particles segmented from the bulk reconstruction. The particles are highly heterogeneous and have complex surfaces.

to be more rounded, although their surfaces retain some irregular features. Closer inspection of an agglomeration of smaller particles reveals that they are highly heterogeneous in shape and their outer surfaces are highly irregular (Fig. 5B). Both of these factors will affect electrochemical performance of the anode during operation through the creation of inhomogeneity in local reaction current densities.

Another consequence of this (Figs. 2 and 5) heterogeneous nano/micro structure is that lithium ion diffusion path lengths will vary throughout the MCMB based anode leading to non-uniform lithium ion intercalation on charging. Having non-uniform path lengths due to different particle sizes and diffusion distances would result in localised regions within the anode experiencing different degrees of intercalation/de-intercalation of lithium ions. Across a lifetime of battery anode operation the cyclic volumetric expansion/contraction generated through small variations in intercalation may lead to mechanical stresses through fatigue. The regions between all the particles imaged in Fig. 5A are expected to be filled with electrolyte and from the imaging data it is therefore apparent smaller particles retain higher surface area to volume ratios, allowing for faster lithium ion diffusion than larger particles.

The anode microstructure was quantified using both in-house and commercial implementations (Tables 1–3); the MCMB anode surface area was found to be $8.55 \times 10^{-4} \text{ m}^2$ for a $3.36 \times 10^{-7} \text{ m}^3$ volume. This reflects a high surface area to volume ratio ca. 3.5 times greater than that for an equivalent sphere of the same volume. Consequently, this would be desirable for fast lithium ion intercalation into the MCMB structure. As a drawback the higher active surface area will result in a larger SEI surface area and therefore more lithium will be consumed irreversibly during SEI formation. In particular from Fig. 5, it is apparent that the smaller MCMB particles which improve connectivity between larger particles have proportionally higher surface area to volume ratio than larger particles, and will therefore play an important role in

determining capacity loss through SEI formation. Altogether the MCMB particles were found to have very high connectivity, being >99% for the anode, with MCMB particles and electrolyte occupying 54.8 vol.% and 45.1 vol.% respectively (Table 1).

The complex shapes formed by MCMB particles and their network (Fig. 5) would influence the lithium ion diffusion rates into, and surface reaction kinetics on, the anode structure. The tortuosity factor can provide a metric towards both measuring MCMB particle shapes and their networks as well as an input towards modelling equations. As such it has been the basis of several studies [6–8,11,12]. Highly tortuous particles also deviate from the idealised spherical based models often used to study battery electrochemistry.

In this study, the microstructure was quantified for both MCMB particle and pore/electrolyte regions via calculation of the tortuosity factor. The tortuosity factor provides a metric towards measuring the inhomogeneity of the particle shape/network and the effective transport properties of the microstructure. In particular, the tortuosity factor was evaluated using two different methodologies. The first technique relies on a random walk method utilising millions of imaginary particles moving through the 3D

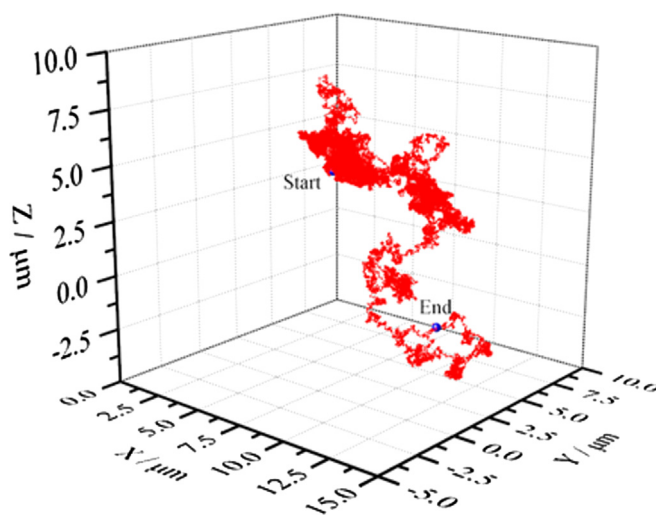


Fig. 6. The random walk of a single imaginary particle through the segmented dataset, shown for the graphite phase. This can be used to calculate mean square displacement and then the tortuosity factor.

Table 1
Microstructural values.

Direction	Graphite	Pore/electrolyte
Volume fractions	54.8	45.1
Connectivity (X/Y/Z)	99.9%	99.8%
Isolated volume fraction	<1%	<1%
Total volume (μm^3)	336	276
Mutual surface area (μm^2)	855	855

Table 2

Random walk based tortuosity factor calculated for both graphite and electrolyte phases.

Direction	Graphite	Pore/electrolyte
X	2.46	2.03
Y	3.69	1.41
Z	6.70	5.72

structure. The mean square displacement can then be used to calculate a measure for the tortuosity factor; further details may be found in Ref. [40]. The second methodology utilises the acquired anode microstructure as a geometric input for finite volume modelling (FVM) of diffusion/conductivity in a set direction. A potential difference was applied across the frontal plane through to the back plane of the MCMB graphite particle microstructure. From the induced flux, a tortuosity factor can be calculated. Further details can be found in Ref. [38]. From both Fig. 6 and Table 2 it is apparent that the path interaction of simulated particles within MCMB/pore regions is strongly dependent on the enclosing microstructure and several times longer than straight diffusion pathways. Similarly Fig. 7 and Table 3 shows the results following conversion of the dataset for FVM analysis and then simulating diffusion through it.

Tortuosity factors for both graphite and electrolyte phases based on the random walk methodology and the diffusion methodology are shown in Tables 2 and 3 respectively. The two methodologies demonstrate excellent agreement for both particle and pore/electrolyte phases in all three directions. The calculations based on the random walk method provide the results at a fraction of the computational expense with considerable computation time saving, in-line with results from previous studies on different electrochemical microstructures [40].

The values clearly show that pathways within the anode structure are tortuous and significantly more so in the z-direction. While these results provide measures of local tortuosity factors, a larger field of view than the present dataset would help to confirm if these differences in value persist or are caused by anode manufacture. Anode preparation methodologies could impart texture e.g. through pressing current collectors against the anode during manufacture. Nevertheless, as smaller MCMB particles occupy space between larger particles (Fig. 5), they also increase the tortuosity factors. The streamlines in diffusion based tortuosity analysis concentrate at contact areas between particles and deviate through small particles increasing effective pathway lengths (Fig. 7) making these regions in the microstructure particularly important to understand. The tortuosity values (Tables 2 and 3) therefore

Table 3

Diffusion simulation based tortuosity factor calculated for both graphite and electrolyte phases.

Direction	Graphite	Pore/electrolyte
X	2.42	2.01
Y	3.56	1.39
Z	6.58	5.61

suggest the greater presence of these small MCMB between larger adjacent particles in the z-direction is likely to be the cause of the increased z-direction tortuosity factors. The presence of the smaller MCMB particles found in this dataset increases effective pathway lengths multiple times as evident from Fig. 7 and given by the tortuosity factors.

Therefore tortuous particles and pores increase diffusion path lengths for both lithium ions intercalating into the MCMB bulk and those travelling in electrolyte filled pores by between 1.4 and 2.6 times for this microstructure. This increased effective diffusion transport length would affect anode performance. When these lengths are considered alongside variation in particle sizes and surface roughness, they would cause inhomogeneous distribution of local salt concentration and lithium in the salt. This would be reflected in local variations in intercalation, current flow and potential. Given the shape and structure of the MCMB particles; it is unlikely that lithium ion intercalation would be homogenous and similarly the SEI layer around particles. Advanced in-situ observational techniques while the battery is electrochemically tested are required to confirm this; however this study provides a useful methodology towards understanding microstructural causes for electrode performance. In doing so the work represents a departure from idealised models generally based on the Bruggeman relationship [41] between porosity and tortuosity factor assuming constant and homogenous thickness of SEI.

4. Conclusions

For the first time known to the authors, it has been possible to image the 3D micro/nano structure of MCMB based anodes (having low Z-numbers) at sub-100 nm resolution using X-ray nano-CT based on enhanced contrast labelling. The contrast labelling technique allowed for the identification of small binder particles in the dataset and binder coatings around MCMB particles. A secondary consequence of labelling was the improvement of contrast at MCMB particle edges aiding MCMB feature segmentation.

The 3D X-ray nano-CT data was consistent with 2D SEM images and showed a bi-modal presence of large MCMB particles (typical

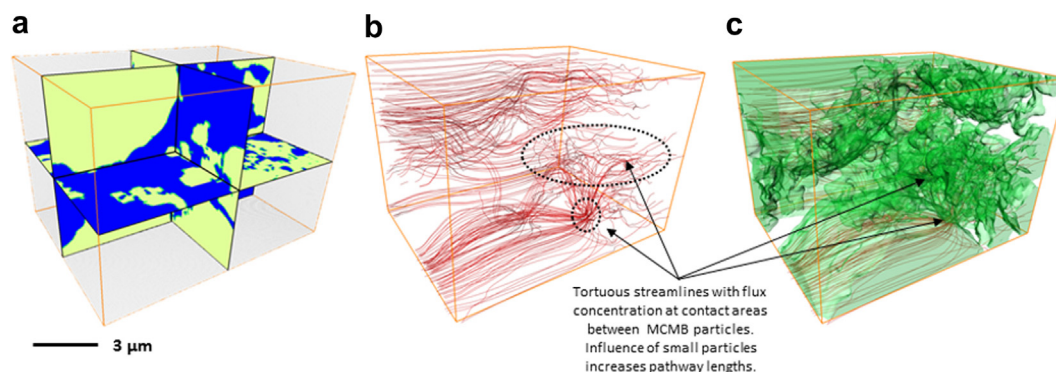


Fig. 7. (a) The geometric input for FVM analysis with cross-sectional slices displayed and (b) complex diffusion pathways through the highly inhomogeneous anode microstructure. Flux concentration is observed at the contact areas between large and small particles, and highly tortuous pathways in small particles as evident with (c) an overlaid anode microstructure.

diameter $\sim 4\text{--}6\text{ }\mu\text{m}$) and small MCMB particles (typical diameter ca. $1\text{--}3\text{ }\mu\text{m}$) based on image contrast and known binder sizes. Small particles frequently filled in gaps between larger particles. Small bright particles (diameter $\sim 0.25\text{ }\mu\text{m}$) are likely to be agglomerated binder/salt particles, while binder was also found coating MCMB particles. Further analysis of the anode would be useful to independently determine the compositional differences between the smallest particles.

A suitable region of MCMB particles from the dataset was successfully analysed and useful metrics such as surface area, volume, connectivity and the tortuosity factor were extracted. These were found to be $8.55 \times 10^{-4}\text{ m}^2$, $3.36 \times 10^{-7}\text{ m}^3$, ca. 99% and between 2 and 7 for the MCMB microstructure respectively. Similarly values for the pore phase were also quantified. Smaller MCMB particles found between larger MCMB particles in this data influences tortuosity factor, causing it to increase. A larger field of view is required to confirm if anisotropy persists. Nevertheless, two different methodologies were used to calculate the tortuosity factor. The random walk methodology was found to be simpler and computationally far less expensive than diffusion based tortuosity calculations while producing consistent results with the latter method. The particles were found to be heterogeneous and have irregular surface structures (hundreds of nanometers surface undulations) which will lead to non-uniform lithium ion intercalation and inhomogeneous SEI in working batteries. The 3D results are complementary to simpler 2D SEM imaging that is unable to provide this insight, which ultimately is important to understand for battery anode performance.

Acknowledgements

All the authors would like to express their gratitude to Xradia Inc. for their continued support that enabled this work to be successfully accomplished. Portions of this research were carried out at the Stanford Synchrotron Radiation Lightsource (SSRL), a Directorate of SLAC National Accelerator Laboratory and an Office of Science User Facility operated for the U.S. Department of Energy Office of Science by Stanford University. The authors gratefully acknowledge support of the beamline scientists. The authors acknowledge funding from the Office of Naval Research Global and Dr. Paul Shearing acknowledges financial support from the Royal Academy of Engineering. Also we would like to acknowledge The Britain Israel Research and Academic Exchange Partnership for financial support and help in organising a fruitful collaboration between the British and Israeli universities. We would like to thank Mr. B. Wu for insightful discussions during the study.

References

- [1] G.-A. Nazri, G. Pistoia, *Lithium Batteries: Science and Technology*, first ed., Springer, New York, 2009.

- [2] E. Peled, D. Golodnitsky, in: P. Balbuena, Y. Wang (Eds.), *Lithium Ion Batteries: Solid-electrolyte Interphase*, Imperial College Press and World Scientific Publishers, 2004, pp. 1–69.
- [3] P. Verma, P. Maire, P. Novák, *Electrochim. Acta* 55 (2010) 6332–6341.
- [4] M. Ender, J. Joos, T. Carraro, E. Ivers-Tiffée, *Electrochem. Commun.* 13 (2011) 166–168.
- [5] J.R. Wilson, J.S. Cronin, S.A. Barnett, S.J. Harris, *J. Power Sources* 196 (2011) 3443–3447.
- [6] T. Hutzenlaub, S. Thiele, R. Zengerle, C. Ziegler, *Electrochem. Solid State Lett.* 15 (2012) A33–A36.
- [7] P.R. Shearing, N.P. Brandon, J. Gelb, R. Bradley, P.J. Withers, A.J. Marquis, S. Cooper, S.J. Harris, *J. Electrochem. Soc.* 159 (2012) A1023–A1027.
- [8] P.R. Shearing, L.E. Howard, P.S. Jørgensen, N.P. Brandon, S.J. Harris, *Electrochem. Commun.* 12 (2010) 374–377.
- [9] F. Meirer, J. Cabana, Y. Liu, A. Mehta, J.C. Andrews, P. Pianetta, *J. Synchrotron Radiat.* 18 (2011) 773–781.
- [10] V. Yufit, P. Shearing, R.W. Hamilton, P.D. Lee, M. Wu, N.P. Brandon, *Electrochem. Commun.* 13 (2011) 608–610.
- [11] D. Kehrwald, P.R. Shearing, N.P. Brandon, P.K. Sinha, S.J. Harris, *J. Electrochem. Soc.* 158 (2011) A1393–A1399.
- [12] R. Thiedmann, O. Stenzel, A. Spetl, P.R. Shearing, S.J. Harris, N.P. Brandon, V. Schmidt, *Comput. Mater. Sci.* 50 (2011) 3365–3376.
- [13] P. Arora, M. Doyle, A.S. Gozdz, R.E. White, J. Newman, *J. Power Sources* 88 (2000) 219–231.
- [14] S.-I. Lee, Y.-S. Kim, H.-S. Chun, *Electrochim. Acta* 47 (2002) 1055–1067.
- [15] S.R. Stock, *Int. Mater. Rev.* 44 (1999) 141–164.
- [16] P. Shearing, D. Eastwood, R. Bradley, J. Gelb, S. Cooper, F. Tariq, D. Brett, N. Brandon, P.J. Withers, P.D. Lee, *Microsc. Anal.* 27 (2013) 19–22.
- [17] M. Ebner, F. Geldmacher, F. Marone, M. Stapanoni, V. Wood, *Adv. Energy Mater.* 3 (2013) 845–850.
- [18] P.R. Shearing, J. Gelb, N.P. Brandon, *J. Eur. Ceram. Soc.* 30 (2010) 1809–1814.
- [19] D. Golodnitsky, E. Livshits, Y. Rosenberg, I. Lapidus, E. Peled, *Solid State Ionics* 147 (2002) 265–273.
- [20] S.J. Riederer, C.A. Mistretta, *Med. Phys.* 4 (1977) 474–481.
- [21] W. Chen, Z. Xu, L. Yang, *J. Power Sources* 102 (2001) 112–117.
- [22] M. Kawakubo, Y. Takeda, O. Yamamoto, N. Imanishi, *J. Power Sources* 225 (2013) 187–191.
- [23] Y. Ito, M. Kawakubo, M. Ueno, H. Okuma, Q. Si, T. Kobayashi, K. Hanai, N. Imanishi, A. Hirano, M.B. Phillips, Y. Takeda, O. Yamamoto, *J. Power Sources* 214 (2012) 84–90.
- [24] S.S. Zhang, *J. Electrochem. Soc.* 159 (2012) A1226–A1229.
- [25] Y. Liu, S. Gorgutsa, C. Santato, M. Skorobogatiy, *J. Electrochem. Soc.* 159 (2012) A349–A356.
- [26] D. Guy, B. Lestriez, R. Bouchet, V. Gaudefroy, D. Guyomard, *Electrochem. Solid State Lett.* 8 (2005) A17–A21.
- [27] Y. Zhang, Y. Zhao, K. Sun, P. Chen, *Open Mater. Sci. J.* 5 (2011) 215–221.
- [28] E. Peled, D. Golodnitsky, G. Ardel, J. Lang, Y. Lavi, *J. Power Sources* 54 (1995) 496–500.
- [29] E. Strauss, D. Golodnitsky, E. Peled, *Electrochim. Acta* 45 (2000) 1519–1525.
- [30] I. Ibanez, W. Schroeder, L. Ng, J. Cates, *The ITK Software Guide*, second ed., Kitware Inc., 2005.
- [31] F. Tariq, R. Haswell, P.D. Lee, D.W. McComb, *Acta Mater.* 59 (2011) 2109–2120.
- [32] R.C. Gonzalez, R.E. Woods, *Digital Image Processing*, second ed., Prentice Hall, Upper Saddle River, New Jersey, 2002.
- [33] M. Petrou, C. Petrou, *Image Processing: the Fundamentals*, second ed., Wiley, Chichester, 2010.
- [34] S. Youssef, E. Maire, R. Gaertner, *Acta Mater.* 53 (2005) 719–730.
- [35] VSG3D, in: 2011.
- [36] M.D. Abramoff, P.J. Magalhaes, S.J. Ram, *Biophotonics Int.* 11 (2004) 36–42.
- [37] K. Martin, L. Ibáñez, L. Avila, S. Barré, J. Kaspersen, *Medical Image Analysis*, vol. 9, Elsevier, 2005.
- [38] M. Kishimoto, H. Iwai, M. Saito, H. Yoshida, *J. Electrochem. Soc.* 159 (2012) B315–B323.
- [39] M. Yoo, C.W. Frank, S. Mori, *Chem. Mater.* 15 (2003) 850–861.
- [40] M. Kishimoto, H. Iwai, M. Saito, H. Yoshida, *J. Power Sources* 196 (2011) 4555–4563.
- [41] D.A.G. Bruggeman, *Ann. Phys.* 5 (1935) 636–679.